Materials Characterization 198 (2023) 112750

Contents lists available at ScienceDirect

Materials Characterization

journal homepage: www.elsevier.com/locate/matchar

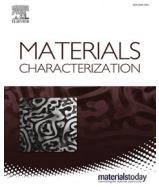

Synchrotron X-ray diffraction analysis of the microstructure of the Ti-6Al-V-Mo-Zr/Al-Cu-Li dissimilar joints produced by CO_2 laser welding

Igor Vitoshkin [a,*], Alexander Malikov [a], Alexey Ancharov [b,c], Artem Filippov [a], Evgenij Karpov [d]

[a] Khristianovich Institute of Theoretical and Applied Mechanics Siberian Branch Russian Academy of Sciences, Institutskaya Str. 4/1, Novosibirsk 630090, Russia
[b] Budker Institute of Nuclear Physics of Siberian Branch Russian Academy of Sciences, Acad. Lavrentieva Pr. 11, 630090, Russia
[c] Institute of Solid State Chemistry and Mechanochemistry, Siberian Branch Russian Academy of Sciences, Kutateladze Str. 18, Novosibirsk 630128, Russia
[d] Lavrentyev Institute of Hydrodynamics Siberian Branch Russian Academy of Sciences, Lavrentyev Ave. 15, Novosibirsk 630090, Russia

ARTICLE INFO

Keywords:
Laser welding
Synchrotron X-ray diffraction
Scanning electron microscopy
Ti alloys
Al alloys
Intermetallics

ABSTRACT

The paper presents the results of both microscopic and synchrotron X-ray diffraction analysis of the microstructure of the dissimilar Ti-6Al-V-Mo-Zr/Al-Cu-Li butt laser welds, as well as their mechanical properties. While the thickness of the welded plates (2 mm), the power (1.2 kW) and velocity (1 m/min) were constant, the variable parameter has been the laser beam offset towards the titanium alloy plate (from 0 to 1 mm). The offset has replaced a conventional joining process (via mixing both molten base metals) into a welding-brazing. The conventional joints have consisted of a separate aluminium melting zone (Al FZ) and a mixing zone (MZ). The Al FZ has contained typical secondary aluminium alloy phases and the $TiAl_3$ intermetallic particles, while the α_2Ti_3Al, β_2-Ti and γTiAl compounds have been found in the MZs. With rising the beam offset value, mechanical tests have shown an increase in the ultimate tensile strength of the welded joints from 74 up to 168 MPa.

1. Introduction

Dissimilar welded joints are of great interest for manufacturers of advanced metal structures because they can combine advantages of different materials. For their fabrication, various welding processes are applied nowadays. In particular, the dissimilar Ti/Al welds are in demand for the aviation industry, since the materials possess low density values and resulting high specific strength levels. Titanium has greater both strength and melting point, while aluminium is characterized by a relatively low cost. However, it is quite onerously to weld these metals, because their physical and chemical characteristics differ significantly. Variations in the chemical properties lead to the formation of intermetallic compounds upon welding. As a result, the dissimilar weld metal has a low capacity for plastic strains and relaxation of residual stresses.

Despite the fact that the dissimilar Ti/Al welds are among the most widely studied to date [1], the majority of investigations has been devoted to alloys of the Al—Mg [2–6] and Al-Mg-Si [7–13] systems. Only a small number of researchers have paid attention to the Al—Li alloys notwithstanding their application in the aviation industry. Therefore, the possibility of obtaining such welded joints is an urgent challenge.

Typically, X-ray diffractometers (XRDs) [3–5] or transmission electron microscopes (TEMs) [10] are used to determine the phase composition. For example, I. Tomashchuk el. al. have investigated fracture surfaces [5], but it still remains unknown which phases have been in the weld metal at a certain depth. In addition, a low intensity of the XRDs does not enable to obtain a sufficiently strong signal from phases containing light elements (lithium, as an instance). Similar issues arise if the phase volume fraction is negligible. The TEMs make it possible to detect phases in such cases, but the completeness of the obtained data is also questionable, since the analysis is carried out in thin foils.

Most studied dissimilar Ti/Al joins have been obtained by welding-brazing procedure. At the same time, investigation of the microstructure of such welds formed by conventional processes (via mixing the molten base metals) is also of interest. Despite both Tomashchuk el. al. [5] and Casalino et al. [7] have showed that such welds possess low strength values, their intermetallic layers have had other phase compositions than those after the welding-brazing procedures. Accordingly, more research is required to fill the gap in knowledge about such interdependencies, which may enable to form sound dissimilar welded joints with improved functional properties.

The use of synchrotron radiation enables to perform various experiments to study porosity, element loss, crack propagation and

* Corresponding author.
E-mail address: igor.vitoshkin.97@gmail.com (I. Vitoshkin).

https://doi.org/10.1016/j.matchar.2023.112750
Received 21 June 2022; Received in revised form 15 December 2022; Accepted 20 February 2023
Available online 22 February 2023

microstructural evolution in weld joints [14–19]. Another way to apply such an instrument to the dissimilar welding studies is to determine diffraction patterns from radiation transmitted through thick samples. Thanks to its high intensity synchrotron radiation diffraction can visualize phases containing light elements, even if their content is low [20], which was performed by L. Chen et al. in [21].

The purpose of our work was to clearly establish the structural composition of the materials obtained in the result of dissimilar welding of Al-Cu-Li and Ti alloys. We noted that the studies on this issue didn't provide the full study of the microstructure obtained in the result of conventional welding – i.e. by direct mixing of the base materials. Existing studies provide X-ray analysis and Transmission electron microscopy (TEM). X-ray analysis doesn't provide necessary signal strength to find the light Li-containing phases and the phases of low volume concentration – Al_3Ti and β_2-Ti in this case. TEM can barely characterize the whole material since the analysis area is tens of nm thick. So we considered the synchrotron X-ray diffraction study as a valuable contribution to the Ti—Al welding issue.

2. Materials and research methods

2.1. Materials

Plates 2 mm thick of the VT-20 (Ti-6Al-V-Mo-Zr) and V-1461 (Al-2.7Cu-1.8Li-0.3 Mg) alloys were used. Their chemical compositions and some physical properties are presented in Tables 1 and 2, respectively.

2.2. Experimental procedure

Before welding, the oxide films had been removed from the plates surfaces by fine grinding. The aluminium plates were further treated with the 10 wt% NaOH aqueous solution.

The plates were butt welded with a CO_2 laser (wavelength is 10.6 μm, beam parameter product was 4.7) at a power of 1.2 kW. At the focus, a laser beam diameter was 200 μm. It was focused with a ZnSe lens at a focal length of 254 mm. The welding speed was 1 m/min. The weld zone was shielded from oxidation with helium gas on both the top and bottom of the weld (Fig. 1, a). The gas is supplied through the nozzle on the top and through the table in the bottom. The nozzle is placed in front of the laser focus and follows it during the welding process. The gas rate was 5 l/min both on the top and the bottom.

Welding was carried out without the beam offset, as well as with the beam offset of 0.5 and 1 mm towards the titanium alloy plate (Fig. 1, c and b, respectively). In all cases, the laser beam was focused at 3 mm below the plate surfaces.

2.3. Research procedures

In this research, both durometric and tensile tests were carried out as well as optical microscopy (OM), scanning electron microscopy (SEM), and the synchrotron X-ray diffraction analysis diffraction (SXRD) analysis were implemented.

The durometric tests were realized with a 'Wilson Hardness' microhardness tester at a load of 0.3 kg according to the Vickers method. At each point, there were four measurements by indentation along 4 parallel tracks.

The tensile tests were carried out with a 'Zwick Roell' tensile testing machine. Samples 100 mm long had a rectangular cross section of 2 × 10 mm.

The OM studies were performed using a 'Olympus Lext 2000' confocal microscope in the non-confocal mode. Cross sections had been alternately etched with Köller's and Kroll's reagents to reveal the microstructure of aluminium and titanium, respectively, as well as with a special solution, containing 5% hydrofluoric acid and 10% HNO_3, for detection of titanium aluminides. After each etching, the OM study was carried out at the corresponding part of the welded joint cross sections.

SEM studies were carried out on an EVO30 XVP microscope equipped with an Oxford Instruments X-Max 80 energy dispersive spectrometer. To determine the chemical composition in the mixing zones (MZs), an energy dispersive X-ray (EDX) analysis was carried at 12 points uniformly distributed over their cross sections.

Diffraction patterns of the welds were obtained at the Institute of Nuclear Physics of the Siberian Branch of the Russian Academy of Sciences at the 4th channel of the 'VEPP-3' station. The beam had a rectangular cross section with dimensions of 400 × 100 μm. The radiation wavelength was 0.3685 Å. The patterns were recorded using a 'mar345' 2D detector located behind the samples (Fig. 2, a), which were circumferentially integrated into spectra then (Fig. 2, b). In this case, only a quarter of the diffraction pattern was used (Fig. 2, c). The distance between the detector and the samples was 425 mm. The detector had a 3450 × 3450 pixels screen with the pixel size of 100 × 100 μm.

3. Results

3.1. Microstructural research

3.1.1. The base metals

The initial V-1461 alloy contained copper-rich (See Table 3) hardening [22,23] precipitates <1 μm in size (Fig. 3, a; points 4 and 6). Also, there were very few larger particles of 6–8 μm (Fig. 3, a; points 1 and 2).

Since the VT-20 alloy belonged to the pseudo-α grade, its microstructure contained a certain amount of the β phase (typically 1–3 vol%). In the studied case, the α phase was observed in both globular and lamellar forms (Fig. 3, c).

The small sizes of the hardening phases in the V-1461 alloy caused their broad and fuzzy reflections in the diffraction patterns (Fig. 3, b). The SXRD analysis of the titanium alloy confirmed the presence of a small amount of the β phase (Fig. 3, d).

3.1.2. Welding without the beam offset

Welding without the beam offset had caused great interaction of the molten base metals, resulting in a wide MZ of about 800 μm (Fig. 4). A part of the molten V-1461 alloy had avoided such intense mixing, so the aluminium fusion zone (Al FZ) was also observed in the microstructure

Table 1
The chemical compositions of the VT-20 and V-1461 alloys.

VT-20										
Ti, wt%	Fe, wt%	C, wt%	Si, wt%	Mo, wt%	V, wt%	N, wt%	Al, wt%	Zr, wt%	O, wt%	H, wt%
Balance	< 0.3	< 0.1	< 0.15	0.5–2.0	0.8–2.5	< 0.05	5.5–7.0	1.5–2.5	< 0.15	< 0.015

V-1461								
Al, wt%	Cu, wt%	Mg, wt%	Li, wt%	Zn, wt%	Zr, wt%	Sc, wt%	Mn, wt%	Ti, wt%
Balance	2.5–2.95	0.05	1.5–1.9	0.2–0.8	0.26	0.28	0.04	0.07

Table 2
The physical properties of the VT-20 and V-1461 alloys.

Alloy	ρ, kg/m^3	λ, W/(m·K)	C_p, J/(kg·K)	T_m, °C	σ_{UTS}, MPa	σ_{YS}, MPa	δ, %
VT-20	4450	8	549	1668	1070	840	10.0
V-1461	2630	92	910	660	550	470	10.1

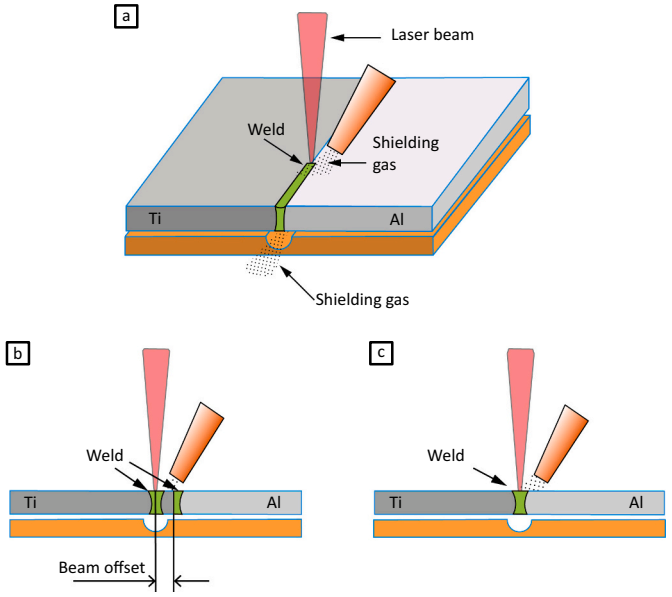

Fig. 1. Scheme of the welding process: a – gas shielding system, b – welding-brazing with the beam offset, c – conventional welding without the beam offset.

of the welded joint.

The Al FZ contained a copper-rich meshed microstructure (Fig. 5, a). According to the SXRD analysis (Fig. 5, b), copper-containing particles included the τ_{1-3} phases that enabled to assess their interconnection with the meshed microstructure. This behavior was typical for this alloy in laser welding and was previously described in [24].

In the Al FZ (Fig. 5, a), the acicular microstructure located independently of aluminium grains. Respectively, it was concluded that they had initially formed from the weld pool. The high titanium content in these particles enabled to suppose their correspondence with the $TiAl_3$ and Ti_2Al_5 phases (Fig. 5, b). However, the Ti_2Al_5 reflections were barely distinguishable in this zone, from which it followed that its content was low. Consequently, such particles were predominantly the $TiAl_3$ intermetallics.

In the MZ microstructure (Fig. 6), small (~1 μm) grains were found, which were surrounded by light areas. It should be noted that β-Ti phase tends to concentrate β-stabilizers (V, Mo and Zr in the studied case), most of which had a higher number in the periodic table (40 for Zr and 42 for Mo vs. 22 for Ti). Therefore, it was assumed that the light areas in the microstructure were residual β_2-Ti inclusions, since they corresponded to heavier elements in the BSD image. Also, this was indicated by the shape of these areas.

In laser welding, a high cooling rate might have caused the fact that the microstructure of the $\alpha_2 + \gamma$ alloy, to which the MZ material had belonged due to its chemical composition (30–34 at.% Al), had transformed into the completely lamellar form [25]. Although it was not possible to detect separately the α_2 and γ phases because of the small amount and/or size of the γ phase, it was concluded that the space between the bright areas was grains consisting of these two phases.

3.1.3. Welding with the beam offset of 0.5 mm

As in the previous case, welding with the beam offset of 0.5 mm had caused intense mixing of the molten base metals, which resulted in the formation of similar both MZ and Al FZ (Fig. 7).

The Al FZ microstructure (Fig. 8) was similar to that after welding without the beam offset, but higher contents of the τ_{1-3} phases, as well as the Ti_2Al_5 and $TiAl_3$ intermetallics were observed.

The MZ microstructure (Fig. 9) was also close to that as in the previous case, but the beam offset of 0.5 mm had resulted in an increase in the aluminium content up to 39–43 at.% that enhanced the γ phase amount.

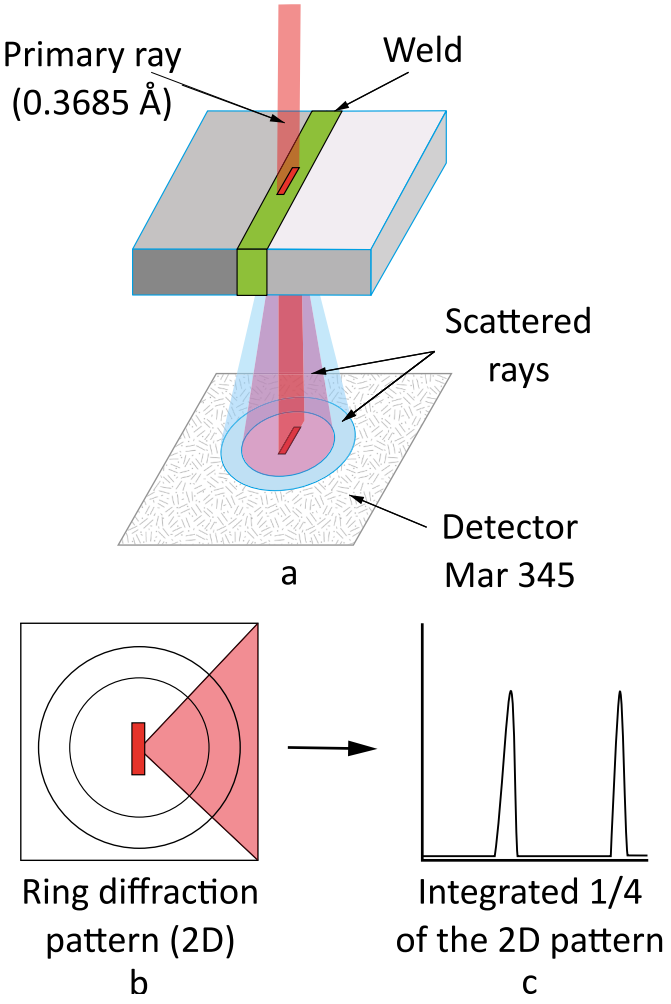

Fig. 2. Flowcharts of the SXRD analysis: a – the research process, b – the used parts of the obtained diffraction images, c –the final spectrum.

Table 3
The chemical compositions at points 1–6 according to Fig. 3, a.

Point	Al, at.%	Cu, at.%
1	87.29	12.71
2	81.08	18.92
3	98.99	1.01
4	97.59	2.41
5	98.67	1.33
6	96.07	3.28

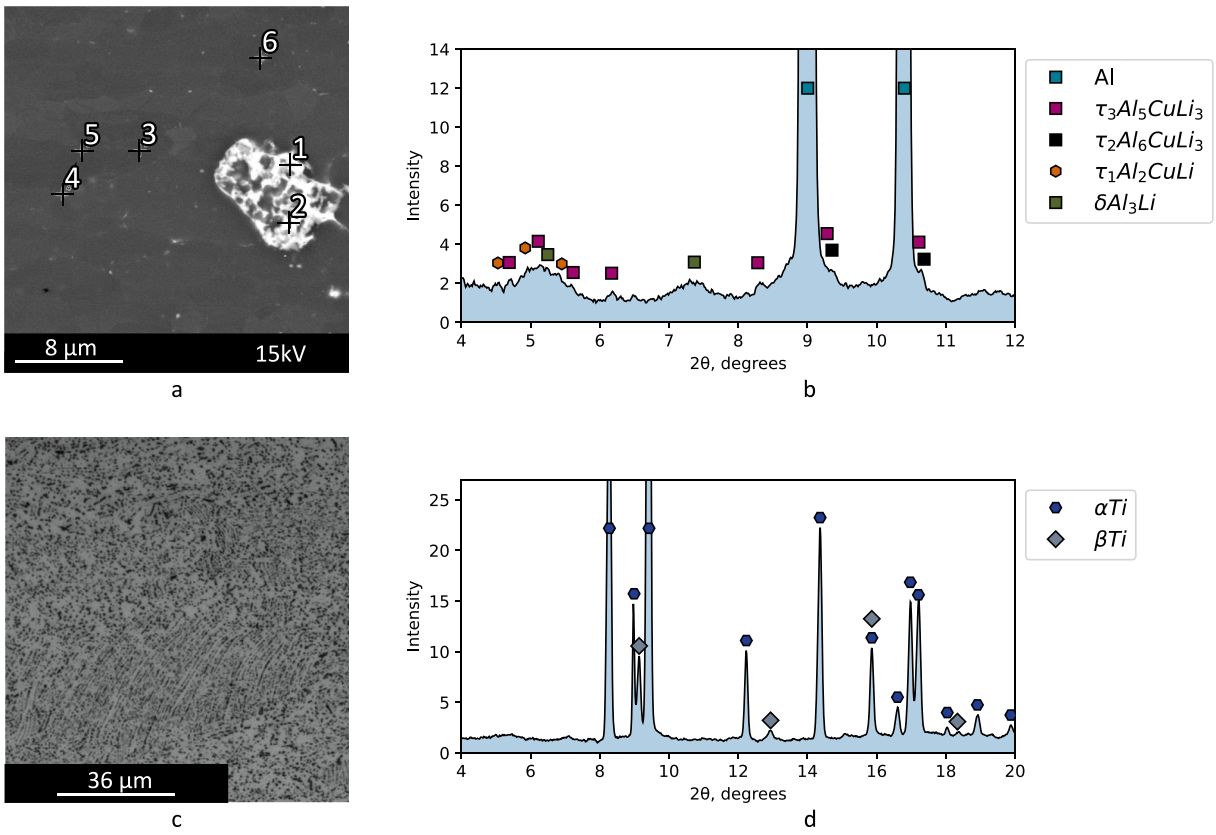

Fig. 3. The microstructure and phase composition of the initial alloys: a – the V-1461 alloy microstructure (SEM, BSD image); b – the V-1461 alloy diffraction pattern; c – the VT-20 alloy microstructure (OM image), d – the VT-20 alloy diffraction pattern.

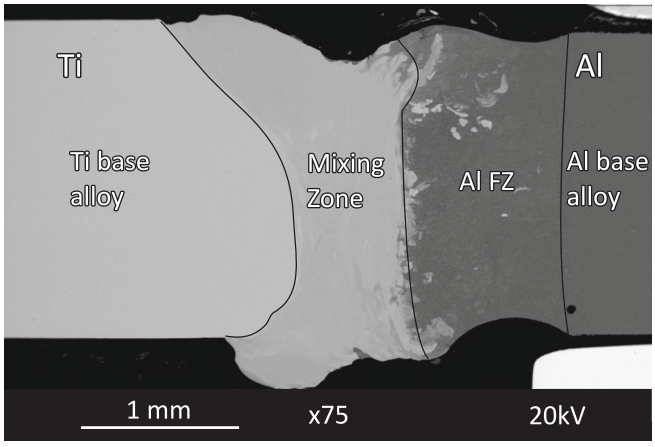

Fig. 4. A general view of the welded joint cross section without the beam offset (BSD image).

3.1.4. *Welding with the beam offset of 1.0 mm*

Welding with the beam offset of 1.0 mm had been enough to prevent intense mixing of the molten base metals, thus avoiding the formation of an extensive MZ (Fig. 10). Instead, two separate (Al FZ and Ti FZ) regions were found on the cross section of the welded joint.

As in both previous cases, melting and subsequent solidification had caused the precipitation of hardening phases at the aluminium grain boundaries, due to which the meshed microstructure surrounding them was found in the Al FZ (Fig. 11, a). The SXRD analysis did not enable to reveal the presence of any Ti—Al intermetallic compounds (Fig. 11, b).

As a result of welding, the VT-20 alloy microstructure had become martensitic (Fig. 11, c). EDX analysis showed an increase in the aluminium content near the interface between the welded plates (15.4 vs. 11.5 at.% Al in the initial V-1461 alloy), which could explain the absence of the β-Ti phase in the SXRD pattern (Fig. 11, d).

At the interface between the welded plates, a clear boundary was observed in the form of an intermetallic layer about 1 µm thick (Fig. 12, a). Near it (Fig. 12, b), the microstructure of the heat-affected zone (HAZ) in the VT-20 alloy plate was similar to that of the base metal (Fig. 3, c). It was concluded from this fact that this area had not been heated enough to allow the formation of a quenching microstructure and, respectively, had not been melted. Since the $TiAl_3$ phase was typically formed during welding-brazing of some Ti/Al parts [2,10], it could be assumed that this intermediate layer consisted of this intermetallic compound.

3.2. *The microhardness tests*

The microhardness test results are shown in Fig. 13. For each group of values, an OM image fragment is given for characterizing them (scales of the images are not the same). In all three studied cases, the microhardness levels of the Al FZs were lower than that of the base metal (~90 vs. 140 $HV_{0.3}$). This could be explained by the release of strengthening particles at the boundaries of aluminium grains. For both beam offset values of 0.5 and 1.0 mm (See Fig. 13a,b), the microhardness levels of about 550 $HV_{0.3}$ in the MZs greatly exceeded other ones at the cross section of the welded joints. On the VT-20 alloy side, welding had resulted in the formation of the HAZ martensitic microstructures, as evidenced by their increased microhardness levels compared to that for the base metal. After welding with the beam offset of 1.0 mm (Fig. 13c), the VT-20 alloy HAZ was characterized by a lower microhardness level compared to that for the base metal with the initial microstructure. This fact enabled to conclude that the VT-20 plate edge had not been heated above the α → β transformation temperature and, respectively, had not

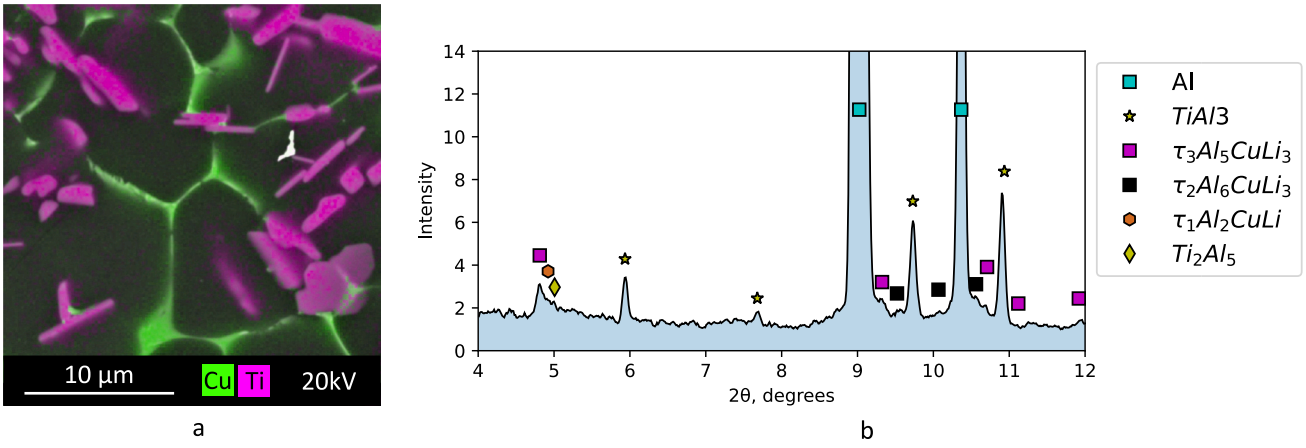

Fig. 5. The Al FZ microstructure without the beam offset (BSD image): a – an EDX map, b – the SXRD analysis results.

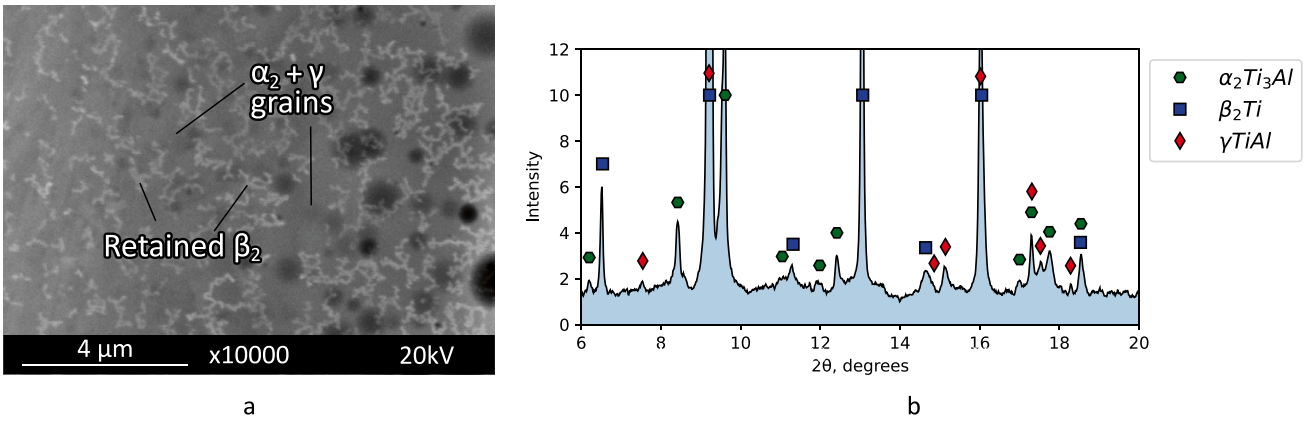

Fig. 6. The MZ microstructure without the beam offset
a – a BSD image; b – the SXRD analysis results.

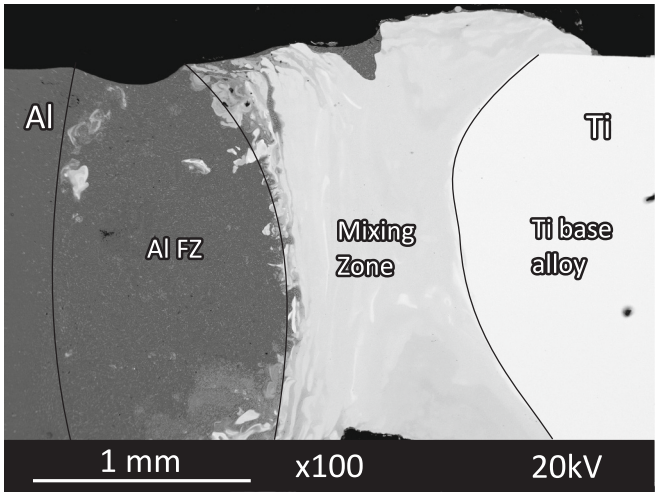

Fig. 7. A general view of the welded joint cross section with the beam offset of 0.5 mm (BSD image).

been melted.

3.3. The tensile tests

The tensile test results showed (Fig. 14) that the beam offset had increased the ultimate tensile strength of the welded joints from 74 MPa (without the beam offset) up to 107 MPa for 0.5 mm, and up to 168 MPa for 1.0 mm.

4. Discussion

The heat input P, energy per height P_{depth}, energy per linear area E_{depth}, energy per volume E were estimated:

$$P = \frac{W}{V} = 72\frac{J}{mm} \quad (1)$$

$$P_{depth} = \frac{W}{t} = 600\ \frac{J}{s \bullet mm} \quad (2)$$

$$E_{depth} = \frac{W}{tV} = 36\frac{J}{mm^2} \quad (3)$$

$$E = \frac{W}{Vth} = 28.81\frac{J}{mm^3} \quad (4)$$

where W is the welding power, V is the welding velocity, t is the thickness of the welded plates, h = 1.48 mm is the average width of the weld.

Upon the weld pool solidification after laser welding, the microstructure formation had been significantly affected by its cooling rate. Two parameters had been dominant at the liquid-solid interface: the *G* temperature gradient and the *R* solidification rate [26]. The formation of dendrites had depended on the *G*/*R* ratio. Since laser welding had been characterized by a very high *R* level, the weld metal of aluminium alloys

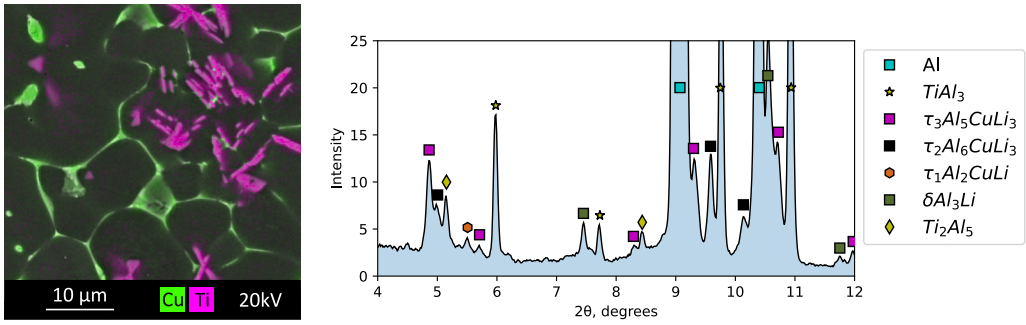

Fig. 8. The Al FZ microstructure with the beam offset of 0.5 mm (BSD image): a – an EDX map, b – the SXRD analysis results.

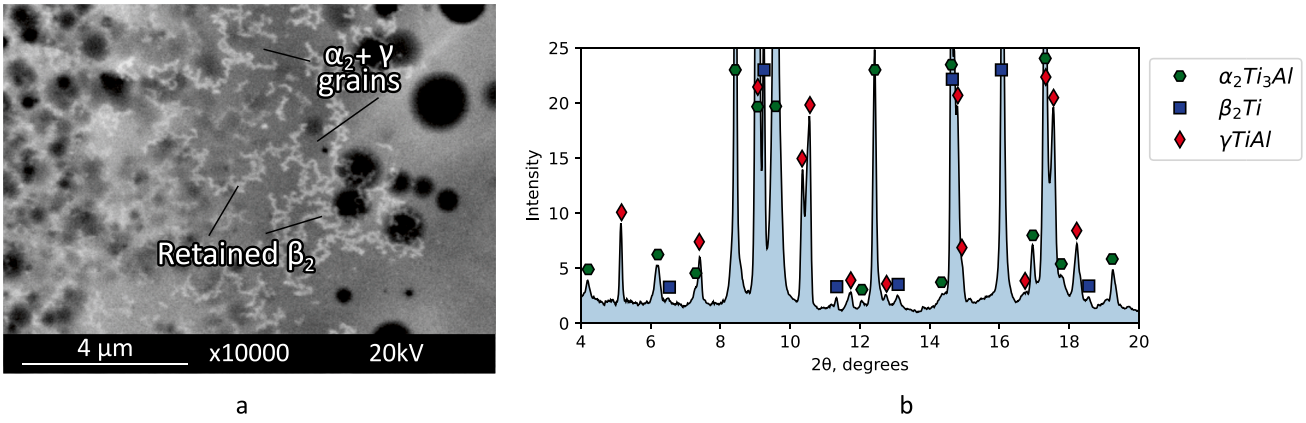

Fig. 9. The MZ microstructure with the beam offset of 0.5 mm:
a – a BSD image; b – the SXRD analysis results.

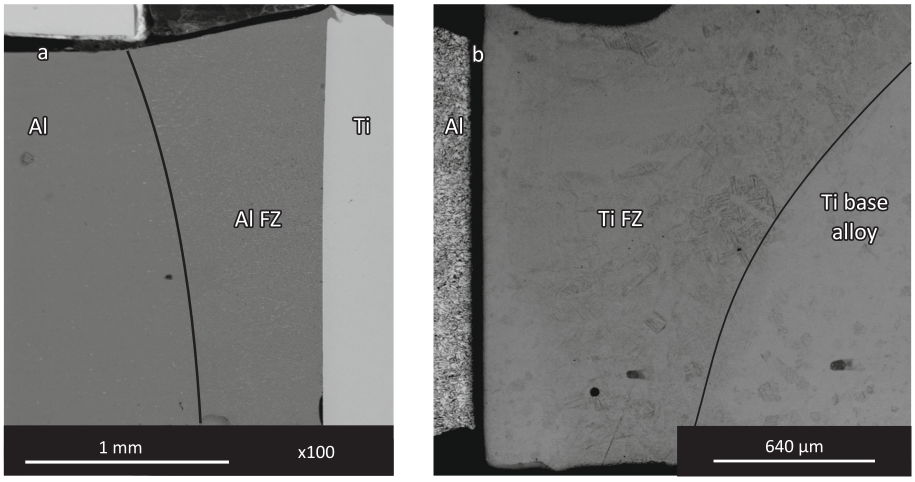

Fig. 10. A general view of the welded joint cross section with the beam offset of 1.0 mm: a – the V-1461 alloy side (BSD image), b – the VT-20 alloy side (OM image).

typically possessed a microstructure composed of such grains. The interrelation of the thermal effect, i.e. cooling rate, with these parameters had been $dT/dt = G \bullet R$. Thus, the G/R ratio had determined the morphology of the grain microstructure. An increase in the cooling rate had caused an acceleration of their nucleation, that is, a decrease in the grain sizes, which had been affected by the $G \bullet R$ multiplication, respectively.

According to [27], the cooling rate in laser welding could be expressed through the following equation:

$$\frac{dT}{dt} = GR = 2\pi \frac{(T_{liq} - T_0)^3}{\eta_{abs}^2 * E_{Depth}^2} \lambda \rho C_p \quad (5)$$

where T_{liq} was the liquidus temperature, η_{abs} was the absorption coefficient of the laser radiation, λ was the thermal conductivity, C_p was the heat capacity, ρ was the metal density, $E_{Depth} = P/tV$ was the laser beam linear energy to the penetration depth.

The cooling rate depended on the λ thermal conductivity and the E_{Depth} linear energy. Respectively, it was possible to estimate the cooling

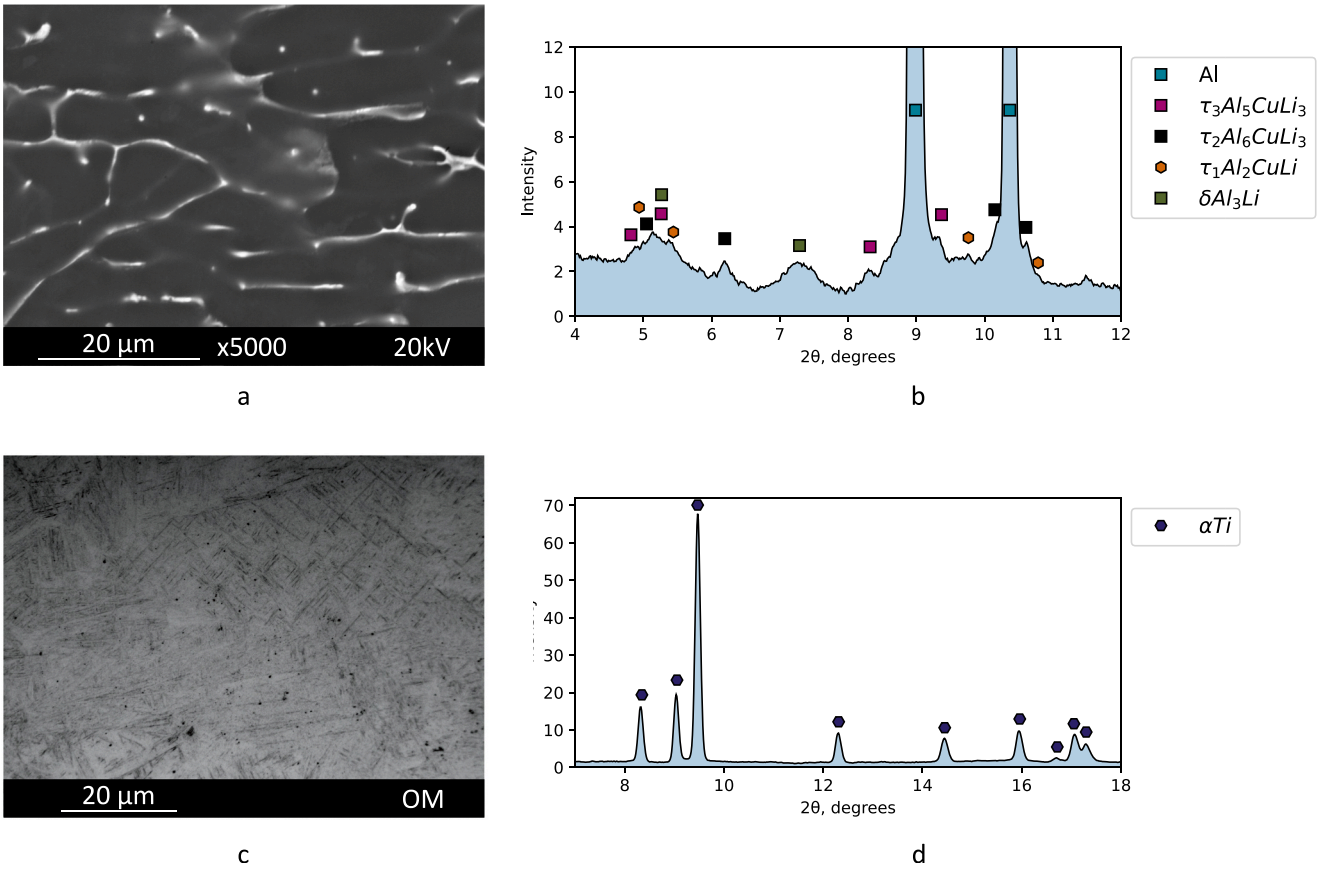

Fig. 11. The Al FZ and Ti FZ microstructures with the beam offset of 1.0 mm: a – a BSD image of the Al FZ; b – the SXRD analysis results of the Al FZ; c – an OM image of the Ti FZ (non-confocal mode); d – the SXRD analysis results of the Ti FZ.

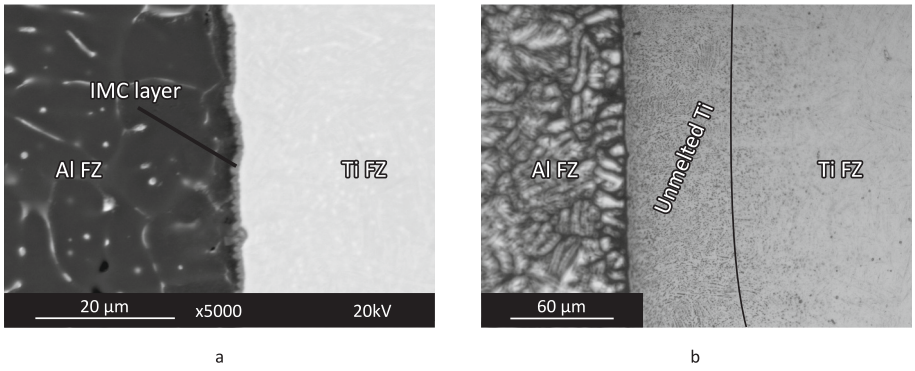

Fig. 12. The microstructure near the interface between the welded pates with the beam offset of 1.0 mm: a – a layer of intermetallic compounds (BSD image); b – a layer of the solid VT-20 alloy between the Al and Ti FZs (OM image).

rate taking into account the process parameters. The cooling rate evaluation results for the joined materials using Eq. 1 with an absorption coefficient of 0.8 gave 1081 K/s for the VT-20 alloy and 1205 K/s for the V-1461 one. As expected, the cooling rate was higher for the aluminium alloy.

According to [27], the solidification rate after laser welding could be assessed via the following expression:

$$G \Big/ R = 2\pi \frac{(T_{liq} - T_0)^3}{\eta_{abs}^2 * P_{Depth}^2} \lambda \rho C_p \quad (6)$$

where $P_{Depth} = P/t$ was the laser beam linear energy to the penetration depth.

The calculation results showed that the G/R ratio was 3.89 K·s/mm^2 for the VT-20 alloy and 4.37 K·s/mm^2 for the V-1461 one (the solidification rate was also greater for the aluminium alloy [28]).

In butt welding, both alloys had been melted and mixed, so it was difficult to apply these estimates. It was stated in [28] that the addition of dissolved or impurity elements in the planar front was beneficial if the temperature gradient was very high and/or the solidification rate was very low. Most of alloys were typically solidified according to the dendritic or cellular type. The local cooling rate had a significant effect on the size (or scale) of the formed microstructure. In this case, high $G{\cdot}R$ values contributed to its refining. The grain shapes were mainly determined by the supercooling degree of the molten material.

The SXRD analysis showed that the welded joints contained the

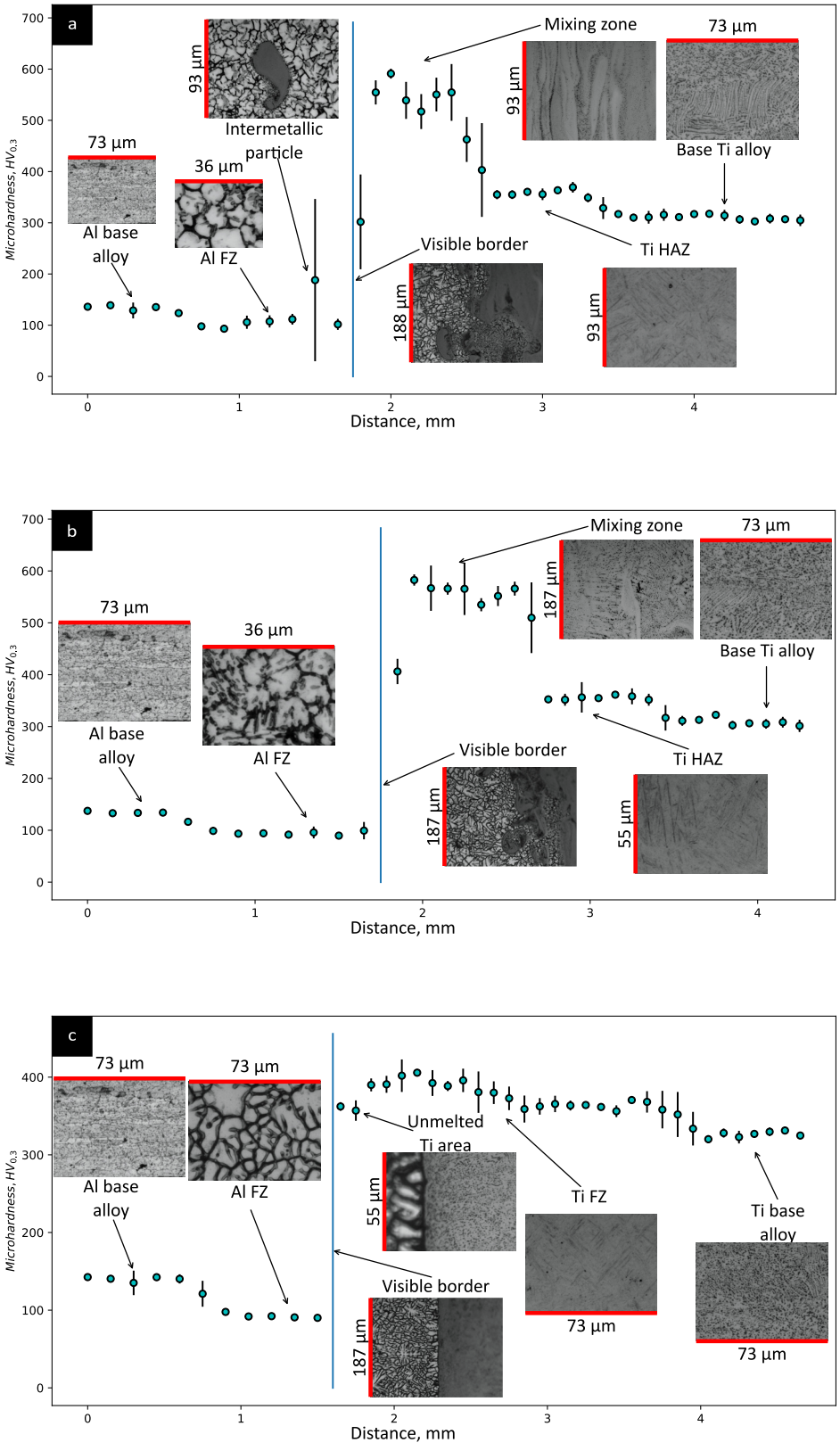

Fig. 13. The microhardness test results: a – without the beam offset; b – with the beam offset of 0.5 mm; c – with the beam offset of 1.0 mm.

$\delta'(Al_3Li)$, $T_1(Al_2CuLi)$, $T_2(Al_6CuLi_3)$, and $T_3(Al_5CuLi_3)$ hardening phases, typical for the V-1461 alloy. Also, the β_2-Ti, α_2Ti_3Al, $\gamma TiAl$, Ti_2Al_5 and $TiAl_3$ compounds were found in addition to the Al, as well as α- and β-Ti phases of the base metals.

The β-Ti phase is characterized by a body centered cubic structure that is stable at temperatures above 882 °C in pure metal or at lower temperature levels in the presence of any β-stabilizing additives such as Cr, Fe, Mo, V, etc. In the studied case, a high amount of Al in the β-Ti solid solution could result in its ordering into the β_2-Ti phase (Fig. 15). Both β_2-Ti and α_2Ti_3Al phases are ordered solid solutions based on the β-

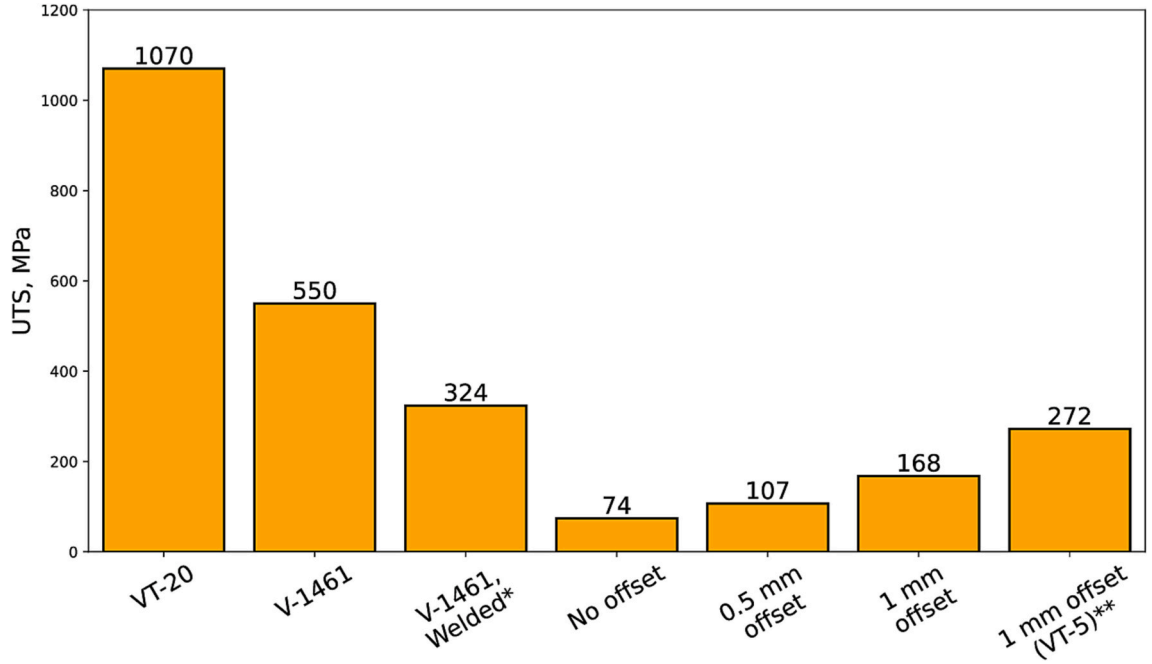

Fig. 14. The tensile test results for the welded joints compared to those for the base metals, as well as similar laser welded joints of the V-1461 alloy* [36] and dissimilar ones with the VT-5 (Ti—6Al) alloy** [37].

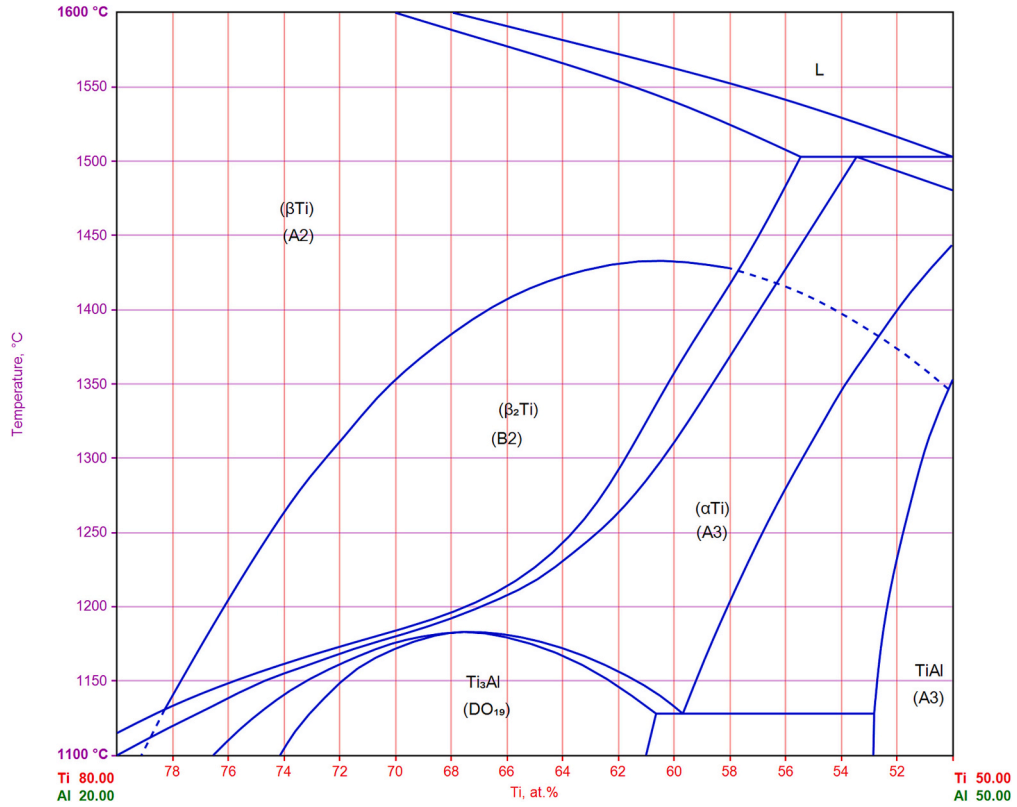

Fig. 15. A part of the Ti—Al state diagram [29].

and α-Ti phases, respectively. The α_2Ti_3Al phase is stable at room temperature without any alloying, while the β_2-Ti phase is stable only at high temperatures (Fig. 15 [29]). This phase can be found at room temperature as a result of alloying with the β-stabilizing elements [30] even at their low total amounts (~3.2 at.% [31]). The γTiAl phase has a tetragonal crystalline structure and can be formed in the Ti—Al solid solutions with an aluminium content of more than ~38 at.% at room temperature. The Ti_3Al phase is also stable at room temperature, but has a very narrow homogeneity range (from 74.5 to 75.0 at.% Al [32]).

In the Al—Li alloys, the $\delta'Al_3Li$ compounds can be formed only as a result of quenching [33] or quenching and subsequent artificial ageing [34]. The T_1Al_2CuLi hardening phase with a hexagonal crystalline

structure is a characteristic of the joined Al-Cu-Li alloy. The $T_3(Al_5CuLi_3)$ and $T_2(Al_6CuLi_3)$ phases are interrelated. The first one possesses a cubic structure, stable in the Al-Cu-Li alloys under normal conditions, while some periodic defects in its structure may cause the formation of the $T_2(Al_6CuLi_3)$ phase with an icosahedral quasi-crystalline structure [35].

According to the Ti—Al state diagram (Fig. 15), the molten alloy containing ~40 at.% Al solidifies at a temperature of about 1550 °C, which had been much higher than the melting point of the V-1461 one (~650 °C). Due to such a significant difference in the melting temperatures, as well as in both cooling and solidification rates, heat had distributed from the solidified MZs into the V-1461 alloy base metal, causing its wider melting. For this reason, the Al FZs were observed in both welded joints, obtained without the beam offset and at its value of 0.5 mm (Figs. 5 and 8). The beam offset of 0.5 mm towards the VT-20 alloy had enhanced a degree of mixing of the base metals. As a result, the MZ included the higher aluminium content (~41 at.% vs. ~34 at.%), and the greater amount of the Ti-containing phases was observed in the Al FZ (Fig. 5, b and Fig. 8, b).

As a result of welding, the microstructure of the V-1461 alloy had been changed significantly, due to which its mechanical properties had greatly deteriorated [36]. Probably, it was possible to return the initial microstructure by post-weld heat treatment, but it would provoke further growth of intermetallic compounds and, consequently, deterioration of the mechanical properties of the welded joints [12].

In the MZ microstructure, the α_2Ti_3Al and $\gamma TiAl$ phases, as well as residual β_2-Ti, were found in the cases of welding without the beam offset and at its value of 0.5 mm. Such inclusions possessed dimensions of <1 μm due to the high cooling rates.

The beam offset of 1 mm had enabled to insulate the molten base metals with the layer of the solid VT-20 alloy. This fact could be estimated from the lower microhardness level in its HAZ near the interface between the welded plates (Fig. 13, c), as well as the similar microstructures in both this region (Fig. 12) and the base metal (Fig. 3, c). Since the $TiAl_3$ phase was typically formed during welding-brazing of some Ti/Al parts, it could be assumed that this intermediate layer consisted of this intermetallic compound [2,10].

5. Conclusions

1. The mechanisms of the microstructure formation in the dissimilar laser welded joints of the VT-20 (Ti-6Al-V-Mo-Zr) and V-1461 (Al-Cu-Li) alloys were reported for both conventional and welding-brazing conditions.
2. At the low beam offset of 0.5 mm and without it at all, laser welding of the VT-20 (Ti-6Al-V-Mo-Zr) and V-1461 (Al-Cu-Li) alloys caused the formation of the wide (0.8–1.0 mm) region, consisting of the α_2Ti_3Al, $\gamma TiAl$ and β_2-Ti phases. The low beam offset of 0.5 mm resulted in enhancing the aluminium content in this region.
3. Welding with the sufficient beam offset (1.0 mm in the studied case) excluded the formation of this zone, replacing it with the thin $TiAl_3$ interlayer.
4. In all studied cases, welding contributed to lowering the strength of the welded joints in the aluminium fusion zone, which could be improved by post-weld heat treatment. The effect of acicular $TiAl_3$ inclusions on the mechanical properties of the welded joints still remains unclear.
5. The beam offset towards the VT-20 alloy improved the ultimate tensile strength of the welded joints from 74 MPa (without the beam offset) up to 107 MPa for 0.5 mm, and up to 168 MPa for 1.0 mm.

Declaration of Competing Interest

The authors declare that they have no known competing financial interests or personal relationships that could have appeared to influence the work reported in this paper.

Data availability

The raw data required to reproduce these findings are available to download from [doi.org/10.17632/r2hhpb6z97.1]. The processed data required to reproduce these findings are available to download from [doi.org/10.17632/fpfjcbgsb2.1].

Acknowledgements

This study was funded by state assignment of Ministry of Science and Higher Education of the Russian Federation (Project No. 121030900259-0). Part of the work was done at the shared research center SSTRC on the basis of the VEPP-4 - VEPP-2000 complex at BINP SB RAS.

Appendix A. Supplementary data

Supplementary data to this article can be found online at https://doi.org/10.1016/j.matchar.2023.112750.

References

[1] S. Kuryntsev, Materials (Basel). 15 (2022) 122.
[2] X. Zhou, J. Duan, F. Zhang, S. Zhong, Materials (Basel). 12 (2019) 712.
[3] P. Leo, S. D'Ostuni, G. Casalino, Opt. Laser Technol. 100 (2018) 109–118.
[4] S. Wei, W. Rao, Z. Li, Y. Zhang, Met. Mater. Int. 26 (2019) 1555–1561.
[5] I. Tomashchuk, P. Sallamand, E. Cicala, P. Peyre, D. Grevey, J. Mater. Process. Technol. 217 (2015) 96–104.
[6] Z. Malekshahi Beiranvand, F. Malek Ghaini, H. Naffakh Moosavy, M. Sheikhi, M. J. Torkamany, M. Moradi, Opt. Laser Technol. 128 (2020), 106170.
[7] G. Casalino, S. D'Ostuni, P. Guglielmi, P. Leo, G. Palumbo, A. Piccininni, Materials (Basel). 11 (2018) 2337.
[8] S. Guo, Y. Peng, C. Cui, Q. Gao, Q. Zhou, J. Zhu, Vacuum 154 (2018) 58–67.
[9] X. Chen, Z. Lei, Y. Chen, Y. Han, M. Jiang, Z. Tian, J. Bi, S. Lin, N. Jiang, Materials (Basel). 12 (2019) 4165.
[10] Z. Lei, P. Li, X. Zhang, S. Wu, H. Zhou, L. Nannan, J. Manuf. Process. 38 (2019) 411–421.
[11] X. Chen, Z. Lei, Y. Chen, Y. Han, M. Jiang, Z. Tian, J. Bi, S. Lin, J. Manuf. Process. 56 (2020) 19–27.
[12] P. Leo, S. D'ostuni, R. Nobile, C. Mele, A. Tarantino, G. Casalino, Metals (Basel). 11 (2021) 1257.
[13] C. Zhang, J.D. Robson, S.J. Haigh, P.B. Prangnell, Metall. Mater. Trans. A Phys. Metall. Mater. Sci. 50 (2019) 5143–5152.
[14] S.C. Wu, Y.N. Hu, H. Duan, C. Yu, H.S. Jiao, Int. J. Fatigue 91 (2016) 1–10.
[15] L. Aucott, D. Huang, H.B. Dong, S.W. Wen, J.A. Marsden, A. Rack, A.C.F. Cocks, Sci. Rep. 7 (2017) 1–10.
[16] S.C. Wu, T.Q. Xiao, P.J. Withers, Eng. Fract. Mech. 182 (2017) 127–156.
[17] T. Nagira, T. Nakamura, F. Yoshinaka, T. Sawaguchi, Y. Aoki, M. Kamai, H. Fujii, A. Takeuchi, M. Uesugi, Scr. Mater. 216 (2022), 114743.
[18] S.C. Wu, X. Yu, R.Z. Zuo, W.H. Zhang, H.L. Xie, J.Z. Jiang, Weld. J. 92 (2013) S64–S71.
[19] M. Rowson, C.J. Bennett, M.A. Azeem, O. Magdysyuk, J. Rouse, R. Lye, J. Davies, S. Bray, P.D. Lee, J. Synchrotron Radiat. 28 (2021) 790–803.
[20] J.P. Oliveira, J. Shen, J.D. Escobar, C.A.F. Salvador, N. Schell, N. Zhou, O. Benafan, Mater. Des. 202 (2021), 109533.
[21] L. Chen, Y.N. Hu, E.G. He, S.C. Wu, Y.N. Fu, Int. J. Light. Mater. Manuf. 1 (2018) 169–178.
[22] L.I. Kaigorodova, D.Y. Rasposienko, V.G. Pushin, V.P. Pilyugin, S.V. Smirnov, Phys. Met. Metallogr. 119 (2018) 161–168.
[23] E.A. Lukina, A.A. Alekseev, L.B. Khokhlatova, M.S. Oglodkov, Met. Sci. Heat Treat. 55 (2014) 466–471.
[24] A. Malikov, A. Orishich, A. Golyshev, E. Karpov, J. Manuf. Process. 41 (2019) 101–110.
[25] X. Wu, Intermetallics 14 (2006) 1114–1122.
[26] S. Kou, Welding Metallurgy, John Wiley & Sons, Inc., 2002.
[27] C. Hagenlocher, F. Fetzer, D. Weller, R. Weber, T. Graf, Mater. Des. 174 (2019), 107791.
[28] J.C. Lippold, Weld. Metall. Weldability (2014) 1–400, 9781118230701.
[29] I. Ohnuma, Y. Fujita, H. Mitsui, K. Ishikawa, R. Kainuma, K. Ishida, Acta Mater. 48 (2000) 3113–3123.
[30] M.H. Loretto, D. Hu, Y.G. Li, Intermetallics 8 (2000) 1243–1249.
[31] V. Imayev, T. Oleneva, R. Imayev, H.J. Christ, H.J. Fecht, Intermetallics 26 (2012) 91–97.
[32] J. Braun, M. Ellner, Metall., Mater. Trans. A Phys. Metall. Mater. Sci. 32A (2001) 1037–1047.
[33] W. Lacom, Zeitschrift Fuer Met. Res. Adv. Tech. 81 (1990) 663–667.
[34] T. Yoshi-Yama, K. Hasebe, M.H. Mannam, J. Phys. Soc. Jpn. 25 (1968) 908.

[35] M. Zinkevich, T. Velikanova, M. Turchanin, Z. Du, M. Materials Science International Team (2014). materials.springer.com/msi/docs/sm_msi_r_10_015854_02.

[36] A.G. Malikov, A.M. Orishich, E.V. Karpov, I.E. Vitoshkin, Mater. Phys. Mech. 43 (2020) 1–10.

[37] A. Malikov, I. Vitoshkin, A. Orishich, A. Filippov, E. Karpov, J. Manuf. Process. 53 (2020) 201–212.